SEPTEMBER 20 2024

Analysis of infrasound array data from tornadic storms in the southeastern United States

Roger Waxler ; Wm. Garth Frazier; Carrick L. Talmadge; Bin Liang; Claus Hetzer ; Hank Buchanan; William E. Audette

J. Acoust. Soc. Am. 156, 1903–1919 (2024)
https://doi.org/10.1121/10.0028815

JASA ARTICLE

Analysis of infrasound array data from tornadic storms in the southeastern United States

Roger Waxler,[1,a] Wm. Garth Frazier,[1] Carrick L. Talmadge,[1] Bin Liang,[1] Claus Hetzer,[1] Hank Buchanan,[1] and William E. Audette[2]

[1]*National Center for Physical Acoustics, The University of Mississippi, University, Mississippi 38677, USA*

[2]*Benchtop Engineering LLC, 281 Sweet Pond Road, Guilford, Vermont 05301, USA*

ABSTRACT:

Data recorded by several infrasound sensor arrays deployed in the southeastern United States during the spring of 2018 have been analyzed during a period when a storm front passed through and spawned several tornado touchdowns. The tornadoes ranged from EF-0 to EF-2. Accurate bearings have been obtained, corresponding to tornadoes at ranges up to more than 100 km. Earlier in the day, a convective storm cell passed and triggered a tornado warning but no verified tornado touchdowns. During this earlier passage, a weaker signal was detected with bearings that tracked this convective storm cell. The analyses reveal that on the systems deployed, the dominant band of coherent infrasound measured from the tornadic storms was between 2 and 6 Hz. Atmospheric conditions are known to have a significant influence on signal detection because of propagation effects and local wind noise conditions. Propagation modeling and wind noise analysis were undertaken and are observed to be consistent with signal detection from the tornadoes. Because of the static sources, as well as the multiple strong cells that were in the region simultaneously, it was necessary to use array signal processing methods that are capable of resolving multiple sources. https://doi.org/10.1121/10.0028815

(Received 26 February 2024; revised 3 August 2024; accepted 3 September 2024; published online 20 September 2024)

[Editor: Andi Petculescu] Pages: 1903–1919

I. INTRODUCTION

Acoustic emissions from tornadic storms have been well documented for some time (Arnold *et al.*, 1976; Bedard, 2005; Elbing *et al.*, 2018; Frazier *et al.*, 2014; Rinehart *et al.*, 2012). Two distinct frequency bands, presumably corresponding to two distinct physical mechanisms, have been identified as relevant to tornado detection: a low frequency audio band and an infrasonic band. There is evidence (Frazier *et al.*, 2014) that the low frequency audible emissions are generated by the turbulence produced by the interaction of a tornado with the ground. An understanding of the mechanism through which the infrasonic signals are generated by tornadoes has remained elusive, although several potential mechanisms have been proposed (Akhalkatsi and Gogoberidze, 2009, 2011; Georges, 1973; Schecter and Nicholls, 2010; Georges and Greene, 1975; Schecter, 2011, 2012; Schmitter, 2010). Nonetheless, these infrasonic signals are readily detected, even from significant distances. See Talmadge and Waxler (2016) for a review.

In this paper, we report on the analysis of data collected on arrays of infrasound sensors deployed in Northern Alabama during the 2018 tornado season. Temporary arrays of purpose-built, low frequency (calibrated 0.01–200 Hz) sensors were deployed at fixed sites in the southeastern United States (U.S.). The sites were chosen in coordination with more traditional meteorological sensor deployments as part of the Vortex-SE program by National Oceanic and Atmospheric Administration (NOAA). The deployments comprised the 2017 and 2018 tornado seasons. Although several storms from the 2017 and 2018 seasons were studied, we have focused on one particular storm, occurring on 19 March 2018, during which there were eight tornado touchdowns confirmed by the U.S. National Weather Service (NWS). Based on the tornado tracks that were published online by the NWS (U.S. Weather Services, 2018), the analysis results from the infrasound data collected indicate continuous detections of tornadoes from out to more than 100 km distance with corresponding accurate direction of arrival (DOA) estimates over time, thus, providing tracks of the bearings from an array to the signal source.

The primary goal of this investigation was to test the hypothesis that all observed tornadoes emit infrasound and then determine what we can learn from the emitted infrasound. As infrasound propagation depends critically on the winds in the atmospheric column, it is highly asymmetric with respect to azimuth (Frazier *et al.*, 2014; Waxler and Assink, 2019; Waxler *et al.*, 2017). For a signal to be detected, the azimuth from the signal source to an array must be one for which propagation is favorable. Further, signals must be detected through the noise generated by the intrinsic, turbulent pressures that accompany atmospheric disturbances, which are generally referred to as wind noise (Raspet *et al.*, 2019). During the passage of a storm, front wind noise levels can become quite high, making signal detection difficult at best and problematic at worst.

[a]Email: rwax@olemiss.edu

Accordingly, the data analyses were augmented by signal propagation modeling to determine which tornadoes one might expect to detect, and the data analysis approach used is one capable of producing estimates of total signal power and total noise power and handling multiple signals arriving simultaneously (Esfandiari *et al.*, 2019).

Despite the high noise levels, multiple signals were detected during the passage of the storm, but due to the noise, little information about the signal waveforms and spectra could be extracted. As a consequence, it was not possible to use the signal waveforms to differentiate between signal sources. Rather, the DOA tracks were used. When tornadoes were present, detections produced bearings which followed the tornadoes, producing continuous and well-defined bearing tracks, sometimes to multiple tornadoes. When tornadoes were not present during the passage of a storm front, signals, presumably from thunder, produced sporadic and scattered bearings; some examples of bearings that tracked non-tornadic thunderstorms can be found in Scamfer and Anderson (2023). An exception was a storm cell of high vertical vorticity, potentially a supercell (Markowski and Richardson, 2011), that generated a tornado warning but produced no verified tornado touchdowns. Continuous and well-defined bearings that tracked this high vorticity cell were obtained, albeit with lower signal power than that for the verified tornadoes.

II. INFRASOUND SENSOR ARRAY DEPLOYMENT

During the spring of 2018 (nominally, February through May), a network of infrasound sensor arrays was deployed by staff of the National Center for Physical Acoustics (NCPA). The network was deployed in northern Alabama, south-central Tennessee, and northwestern Georgia. The Vortex-SE program involves several research groups primarily employing traditional meteorological sensors (radars and lightning detectors) to study tornadoes in the southeastern U.S.. The arrays were separated into two groups of five, and the locations were selected based on guidance from Vortex-SE program meteorologists, site availability, and access considerations. The goal was to surround and provide coverage of the two regions selected by the Vortex-SE meteorologists for focused analysis. In this paper, we focus on one of the regions, referred to as the Western Domain, which is located in north-central Alabama around Huntsville. A map of the infrasound array network, as well as the tracks of the tornadoes studied, is provided in Fig. 1.

The sensing elements are the NCPA designed prototypes of sensors commercially available from Hyperion Technology Group, Inc. They have calibrated responses from approximately 0.01 Hz to 200 Hz and possess built-in Global Positioning System (GPS) receivers for location and timing information, as well as built-in 24-bit data acquisition systems. These sensors do not have data transmission capability; the data are stored on the sensor and must be visited to be retrieved. Power is supplied by batteries with solar cell augmentation. The sensors were set to record 1000 samples per second, and semi-hemispherical porous dome wind screens (Raspet *et al.*, 2019) were used for wind noise reduction. The domes are constructed at NCPA and provide up to 20 dB signal-to-noise ratio (SNR) improvement in the infrasonic band above 2–3 Hz. Two types of domes were used, older cloth-clad domes and more recently constructed

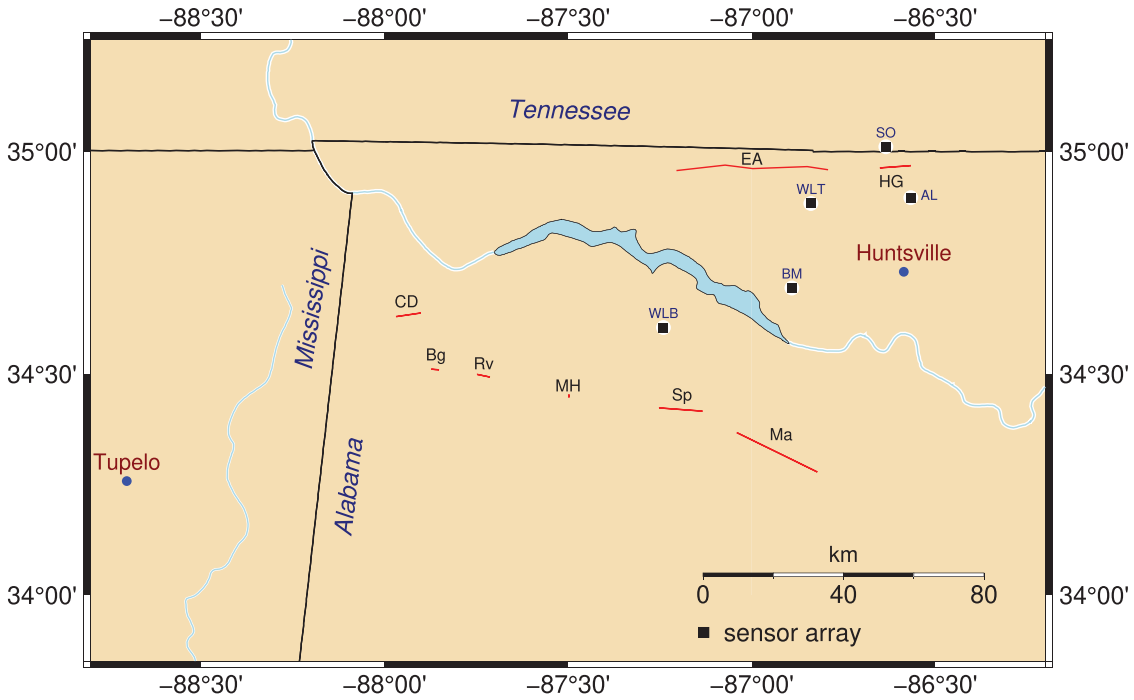

FIG. 1. Infrasound sensor array network as deployed near Huntsville, Alabama and tornado paths for the afternoon of March 19, 2018 as determined by the NWS; see Table I. The infrasound sensor arrays are indicated by the black squares, and the tornado paths are indicated by the red lines.

https://doi.org/10.1121/10.0028815

TABLE I. List of tornadoes on March 19, 2018.

Tornado (abbreviation)	Rating	Start time	Stop time
Coon Dog (CD)	EF-1	17:05	17:15
Belgreen (Bg)	EF-0	17:10	17:16
Russellville (Rv)	EF-1	17:21	17:30
Mount Hope (MH)	EF-0	17:54	17:56
Elkmont-Ardmore (EA)	EF-2	18:08	18:46
Speake (Sp)	EF-1	18:18	18:22
Massey (Ma)	EF-1	18:29	18:59
Hazel Green (HG)	EF-1	18:58	19:04

aluminum-clad domes. Both types provide similar SNR improvement, however, the cloth domes are more fragile.

The infrasound sensor arrays were designed to provide coverage of the two frequency bands that had previously been identified as significant: an infrasonic band of 1–10 Hz and a low frequency audible band of 20–175 Hz (Arnold *et al.*, 1976; Bedard, 2005; Frazier *et al.*, 2014). Nominally, the arrays deployed consisted of eight sensors. They were designed to form two nested subarrays: a four-element square infrasound array, approximately 100 m on a side, and a triangular subarray of closely spaced sensors, approximately 5 m apart, in the interior. A single sensor outfitted with porous hose wind noise reduction was also deployed. The porous hose equipped sensor was intended for deep infrasound such that its location is not critical; the data collected on the porous hose equipped sensors will not be discussed here. In this paper, we will focus only on the 1–10 Hz band and, hence, will only report on data analysis for the large aperture subarrays. In practice, due to topographical considerations, it was not possible to deploy arrays to conform to a consistent geometrical design.

Experience gained from observations has revealed that this network configuration is not optimal, at least for the tornadoes that occurred on 19 March 2018. Most of the storm cells traveled from the west to the east or even from the west-northwest to the east-southeast. Furthermore, as the propagation analysis to be discussed in this paper has revealed, dominant propagation was from west to east. It follows that to detect a signal on an array, it must be to the east of the signal source. Therefore, a network that is elongated more from the west to the east, likely, would have proven more beneficial as the storm cells moved through the area, allowing sound from the tornadic storms to have been detectable over longer periods of time. In subsequent deployments, this strategy has been adopted. We also found that the 100 m aperture was not ideal as it is tuned to the low part of the infrasonic band, which is a bit less than 3 Hz. In subsequent deployments, the aperture has been reduced to about 50 m, putting the ideal detection frequencies in the middle of the 1–10 Hz infrasound band of interest.

III. SUMMARY OF CONDITIONS ON 19 MARCH 2018

Two bands of storm cells, often referred to as squall lines, passed through northern Alabama on March 19, 2018. The first band of storms passed through in the afternoon and triggered a tornado warning; however, the NWS reported no verified tornado touchdowns. The second band of storms passed through in the evening and was larger and more active. It triggered several tornado warnings, and the NWS reported eight confirmed tornado touchdowns within a 100 min period. The tornadoes ranged in intensity from EF-0 to EF-2. A list of these tornadoes is provided in Table I.

In Fig. 1, a map shows the nominal paths of the tornadoes and locations of the arrays comprising the western group: west left top (WLT), Alabama A and M (ALAM), Scott Orchard (SO), Belle Mina (BM), and west left bottom (WLB). Two tornadoes, Elkmont-Ardmore (EA) and Hazel Green (HG), passed through the northern part of the array group. The other six tornadoes were part of a string of cells that passed to their south. The BM array was dysfunctional at the time because of prior submersion of most of the sensor elements as a result of flooding of the low-lying terrain in the area. The remaining four arrays were purposeful; however, all of these arrays had reduced functionality because of the loss of sensor elements for reasons ranging from flooding to damaged cables and solar panels. The functional configurations of the four remaining arrays are displayed in Fig. 2. The porous hose equipped sensors are not considered as the signal attenuation in the analyzed frequency band of 1–10 Hz is too great.

Figures 3 and 4 provide radar images obtained from Iowa State University's Iowa Environmental Mesonet website (Iowa State University Department of Agronomy, 2024), corresponding to the data analysis period 0100–2000 central daylight time (CDT). The underlying maps are

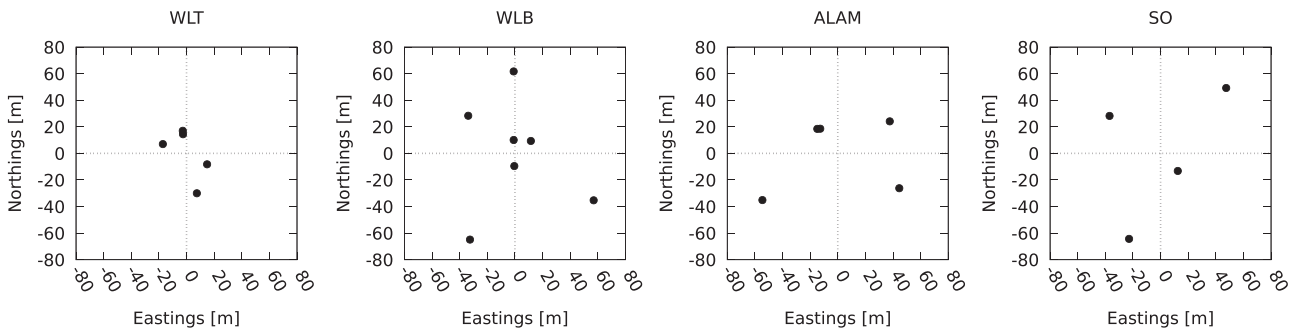

FIG. 2. Functional array configuration of the four arrays on March 19, 2018. The locations of the porous hose equipped sensor are not shown.

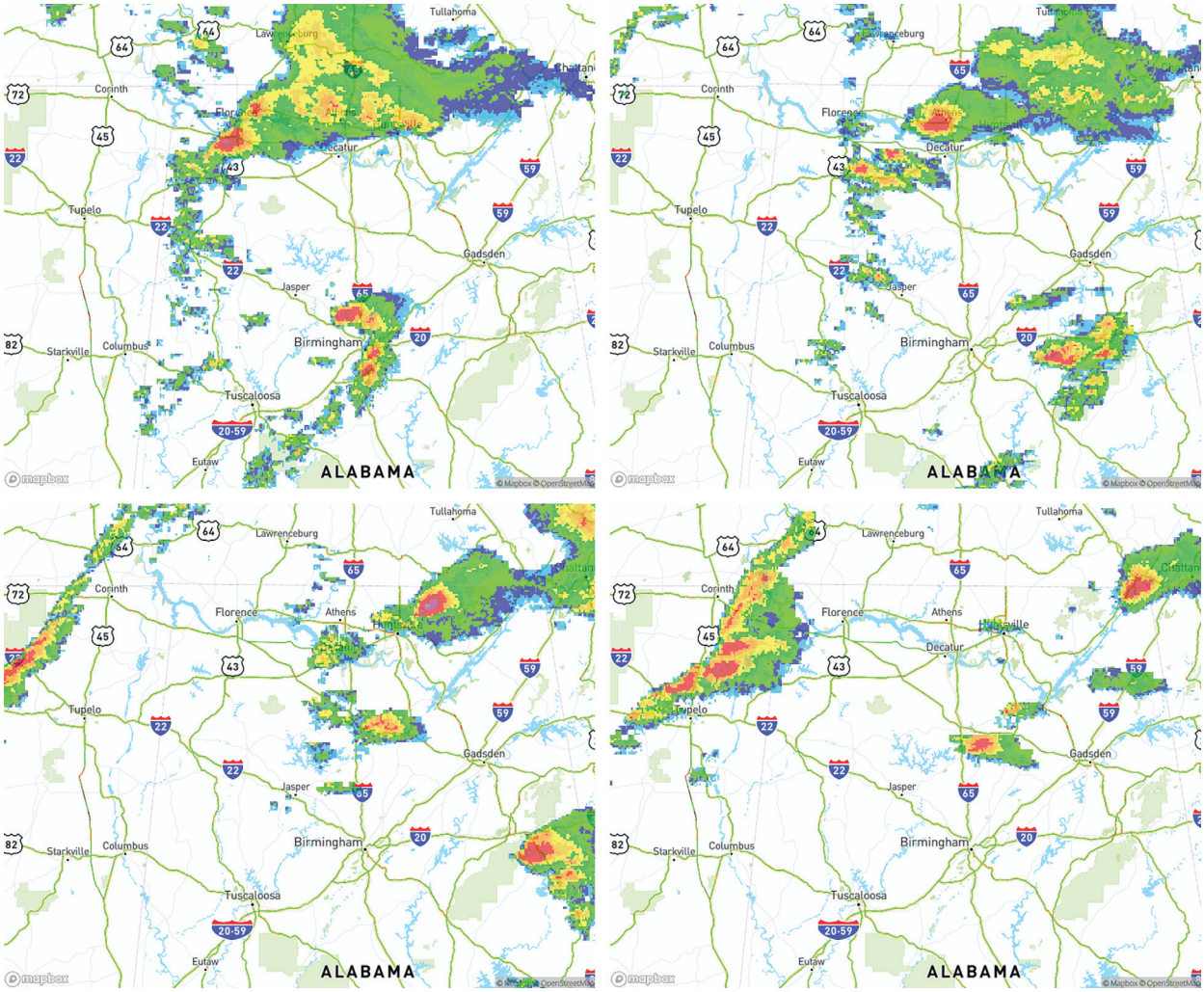

FIG. 3. Passage of a supercell storm front over northern Alabama in the afternoon of March 19, 2018. Radar images are shown every 60 min starting at 1330 CDT and ending at 1630 CDT. A single tornado warning was triggered at about 1340 CDT by the cell observed passing to the south of Florence, Alabama at 1330. The NWS did not report any verified tornado touchdowns.

produced using data made available by Mapbox (2024) and OpenStreetMap (2024). The images clearly show how the storms traverse the region where the arrays were deployed and reveal the very heavy rainfall associated with the storm. In Fig. 3, the first set of storm cells is shown. The cell that triggered the warning is observed in the first image at 1330 CDT, passing to the south of Florence, Alabama, after which it moved to the east-northeast, passing to the north of Decatur and then Huntsville before moving out of Alabama and heading toward Chattanooga, Tennessee. The second set of storm cells can be seen beginning to cross the Mississippi/Alabama state line. In Fig. 4, the second set of storm cells is depicted. Two strings of cells are visible, the one that spawned the EA and HG tornadoes is spotted passing to the north of Decatur and Huntsville, and the cells that spawned the other six tornadoes are viewed passing to the south of Decatur and Huntsville. After 20:00 CDT, most of the storm system had moved east of the array locations, but some cells were still nearby to the south and southwest; as will be demonstrated in the analysis of the infrasound propagation conditions, once the storms passed to the east of the arrays, any acoustic emissions that might have been emitted would not have been able to reach the arrays.

Tornado ground tracks relative to the array positions are shown in Fig. 1. The ground tracks were not precisely evaluated but calculated as straight lines from point of touchdown and point of liftoff as reported on websites maintained by the NWS (U.S. Weather Services, 2018). Overall, distances between the tornadoes and the arrays range from almost 140 km to less than 10 km. There were periods of time when more than one tornado was on the ground simultaneously. Figure 1 reveals that the E-A tornado passed by the WLT array with a closest point of approach just under 10 km from the array.

Of principal importance for the propagation of infrasound signals are the vertical atmospheric profiles of wind and temperature (Waxler and Assink, 2019). Humidity plays a role in the attenuation, but its influence on the effective soundspeed profile is not significant and generally swamped by the uncertainties in the wind velocity. An example profile

https://doi.org/10.1121/10.0028815

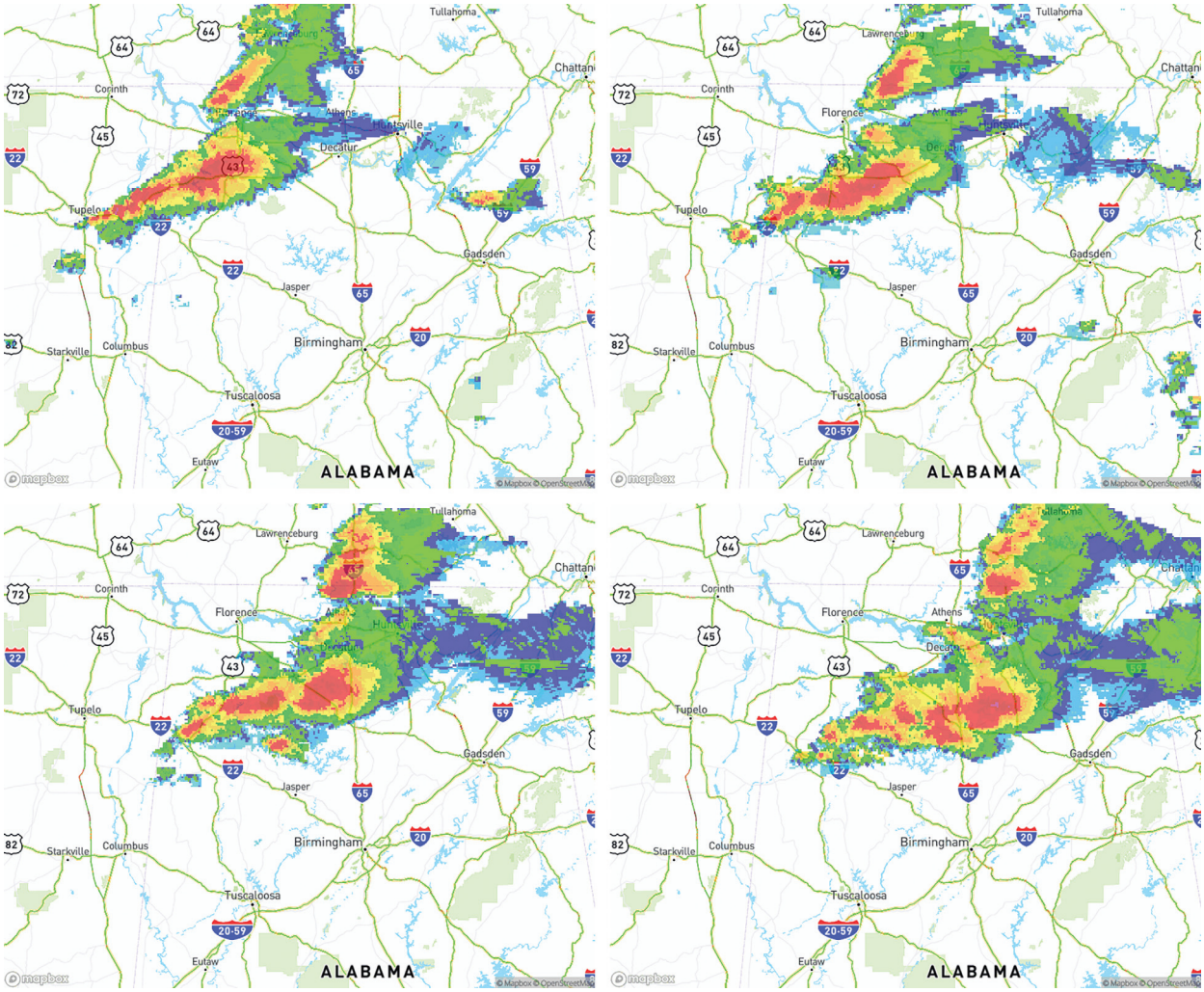

FIG. 4. Passage of a supercell storm front over northern Alabama in the evening of March 19, 2018. Radar images are shown every 30 min starting at 1730 CDT and ending at 1900 CDT. Multiple tornado warnings were triggered. The NWS reported eight verified tornado touchdowns.

is shown in Fig. 5; it is the profile given by the Weather Research and Forecasting (WRF) hindcasting model (Skamarock *et al.*, 2019) above the EA tornado at the time of onset. The atmospheric temperature and wind profiles were qualitatively similar across the area during the storms. The predicted signal attenuation (transmission loss) for ground-to-ground propagation of a 4 Hz signal is also revealed. One sees that conditions were generally downward refracting for propagation from the source to a wedge ranging from southeast to north-northwest. This means that signals would have reached a particular array from source azimuths ranging from south-southwest to northwest. In addition, there was a temperature inversion at the time just barely visible in the sound speed profile in Fig. 5. The terrain in the area consists of rolling hills and is a mixture of farmland and small towns with a dominance of densely forested regions. No large terrain features were located between the tornadic storms and the sensor arrays.

IV. CONSIDERATIONS OF SIGNAL AND NOISE

Other than the strength of an infrasonic source, the most significant factors in detecting a signal from the source are propagation from source to sensor array and noise at the sensor array. In this section, the signal propagation from each tornado to each array is studied, and the noise conditions at each array are analyzed.

Infrasound propagation is strongly dependent on the winds in the atmospheric column and, thus, highly asymmetric with respect to azimuth. As observed in Fig. 5, under the conditions that were prevalent on the evening of March 19, 2018, the infrasound signal propagation was almost binary. For a given azimuth from source to sensor array, the array is either in a well ensonified region or an acoustic shadow zone in which signal strength in almost guaranteed to be far below the background noise levels. The transition zone between the two regions is quite narrow.

The noise at an array is almost always dominated by wind noise or local turbulent pressure fluctuations in the atmosphere surrounding the sensors (Raspet *et al.*, 2019). The wind noise can be quite significant and is often the greatest impediment to infrasound signal detection, frequently being large enough to obscure the signal one is attempting to detect. Wind noise levels are known to depend strongly on location, time of year, and time of day (Bowman

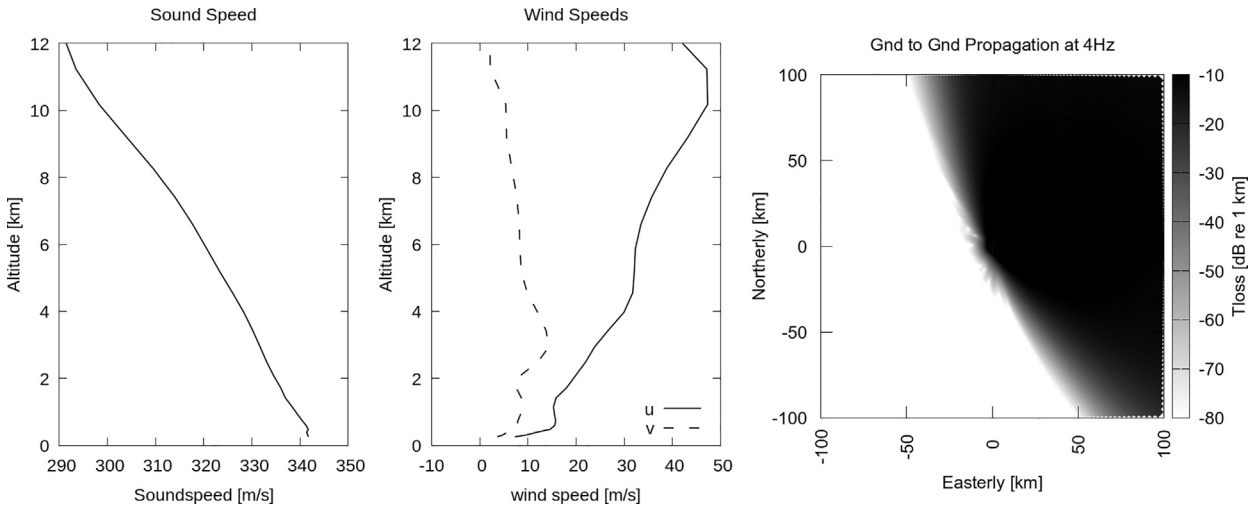

FIG. 5. Atmospheric sound speed and wind speeds above the EA tornado at the time of onset, where u and v denote easterly and northerly wind speeds, respectively. The attenuation of a 4 Hz signal from a source on the ground to a receiver on the ground is shown in the rightmost panel. The profile is the WRF hindcast.

et al., 2005; Marty, 2019). Studies of the relation between topographical features and wind noise levels are in their infancy (Frazier *et al.*, 2024).

A. Signal propagation analysis

As discussed above, infrasound signals propagate efficiently downwind in ducts produced by vertical wind shear. Upwind from a source, the signal is refracted upward away from the ground. We introduce a quantity that we will call reception loss, which is the signal attenuation relative to a receiver. The reception loss for a signal produced by a source at position $\mathbf{r}_S$ to a receiver at position $\mathbf{r}$ is simply the transmission loss (the magnitude of the signal attenuation in dB relative to one) for propagation from $\mathbf{r}_S$ to $\mathbf{r}$. In Fig. 6, reception loss at 5 Hz for the WLT array during the EA event is shown under the assumption that the atmosphere is vertically stratified. In this case, reception loss is given, using the principle of generalized reciprocity (Godin, 1997), by computing the Green's function for signal propagation, then, exchanging source and receiver locations, and reversing wind direction. For a vertically stratified atmosphere, if $G(\mathbf{v}, \mathbf{r}_S, \mathbf{r}, \omega)$ is the signal at angular frequency ω, produced at position $\mathbf{r}$ by a unit point source at position $\mathbf{r}_S$, then

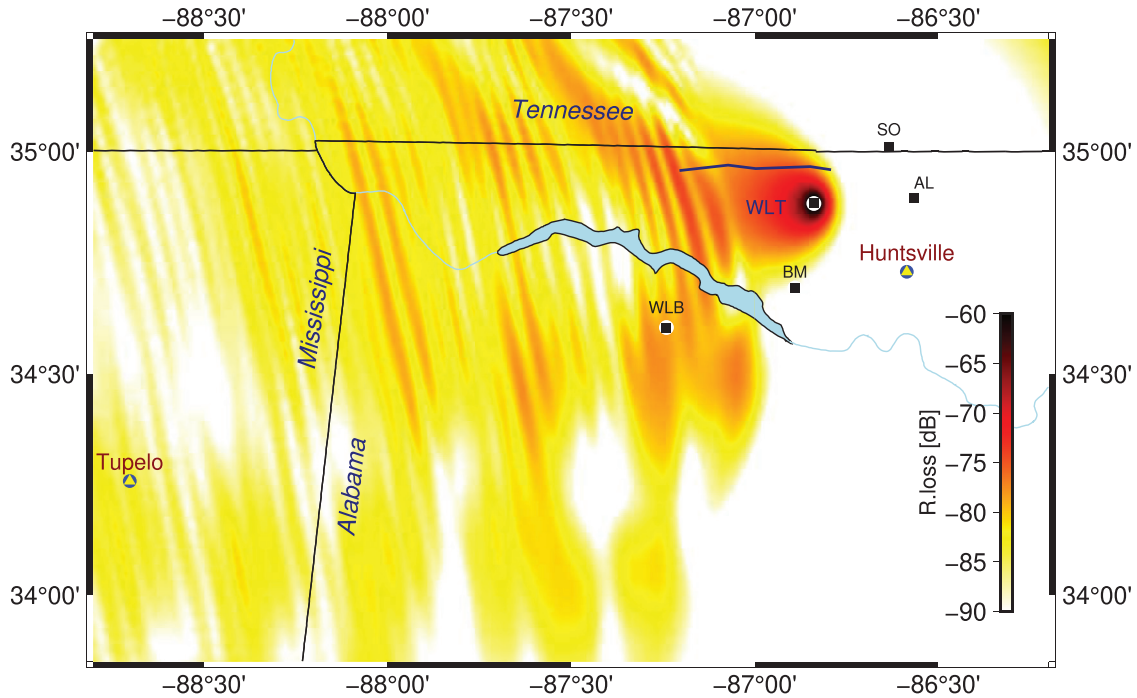

FIG. 6. Ground to ground reception loss at 5 Hz to the WLT array at the time of the EA tornado. The track for the EA event produced by the information provided by the NWS is depicted in blue. For this model, a single atmospheric profile is used. Propagation is modeled with a parabolic equation (PE) model.

https://doi.org/10.1121/10.0028815

$$G_R(\mathbf{v}, \mathbf{r}_R, \mathbf{r}, \omega) = G(-\mathbf{v}, \mathbf{r}, \mathbf{r}_R, \omega)$$

is the signal received at $\mathbf{r}_R$ from a unit point source ar $\mathbf{r}$. We define the reception loss as the magnitude of G_R, expressed in dB relative to one. G_R (times the response function of the infrasound sensor) may be thought of as the acoustic response of the combined system of sensor and atmosphere. If $S(\mathbf{r}, \omega)$ is the acoustic source strength, then the acoustic pressure at a point $\mathbf{r}_R$ is given by

$$P(\mathbf{r}_R, \omega) = \int G_R(\mathbf{v}, \mathbf{r}_R, \mathbf{r}, \omega) S(\mathbf{r}, \omega)\ d^3r.$$

In the absence of a model for the acoustic source of a tornado, we will assume that it is a point source on the ground with the understanding that results are likely to be only qualitative. As discussed previously, Fig. 6 shows that the WLT array was sensitive, depending on signal strength and local noise levels, to signals emanating from points in a wedge to the west from south-southwest to north-northwest. The track for the EA tornado is shown in Fig. 6 in blue. Note that, until the very end, the track is in the region where efficient propagation to WLT is expected. At the end of the track, the tornado enters an acoustic shadow zone relative to WLT.

The propagation conditions from each of the considered tornadoes to each of the functional arrays have been studied. The atmospheric profiles change with time as well as with range. Assuming that each tornado has been traveling at a constant speed, at each 5 min interval along each tornado's path, the set of propagation paths from tornadoes to arrays is defined. Along each propagation path, atmospheric profiles were collected every 5 km from atmospheric models calculated using WRF (Skamarock *et al.*, 2019) and obtained from the WRF archive NCEP/NWS/NOAA (2015). The sets of profiles were input into a parabolic equation (PE) propagation model (Collins and Siegmann, 2019; Waxler *et al.*, 2021) to estimate the attenuation, as a function of time, of the infrasound signal as it propagates to each array.

Consider the propagation of signals from the EA tornado to the WLT array. The initial touchdown for the EA tornado was reported to begin at about 18:08 U.S. Central Standard Time (CST) and ends at about 18:46 CST. In Fig. 7, the transmission losses along each of the paths from the EA tornado to the WLT array are plotted. Consistent with the results depicted in Fig. 6, propagation from EA to WLT is efficient at first, but as the tornado passes by to the north of the array, the signal attenuation is predicted to increase dramatically, even while the range from tornado to array decreases. Note that the transmission loss values at the end of each curve in Fig. 6 are the reception losses at WLT from the corresponding point on the tornado track.

This same analysis was performed for all array/tornado pairs. In Fig. 8, the resulting reception losses at each of the arrays from each of the tornadoes are shown. One observed that signal propagation to the SO and ALAM arrays was favorable for all of the tornadoes in the sense that neither

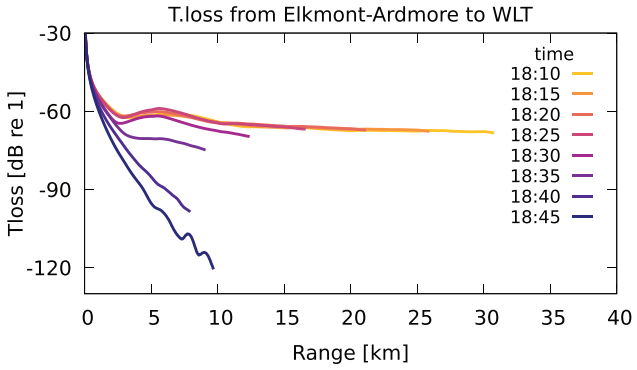

FIG. 7. Signal attenuation for ground-to-ground signal propagation at 4 Hz from the EA tornado track to the WLT array over time.

SO nor ALAM were ever in acoustic shadow zones for any of the tornadoes. At WLB, propagation conditions were favorable for detection only from the Mount Hope, Russellville, and Speak tornadoes. At WLT, propagation conditions were favorable for detection from the Massey, Mount Hope, Russellville, and Speak tornadoes for the entirety of their tracks and from the EA tornado until it passed by the array to the north. Given the propagation conditions depicted in Fig. 5, these results are in qualitative agreement with the relative positions of the arrays and tornadoes as shown in Fig. 1.

B. Wind noise analysis

To evaluate the wind noise levels at the four functioning arrays, 6 weeks of data from March 1 through April 11, 2018 were analyzed. The root mean square (RMS) of the pressure at each sensor was computed in 5 min intervals to track the noise pressure levels over time. To compute the RMS pressures, the data were first downsampled to 100 sps. Then, the power spectral densities (PSDs) were estimated every 5 min using a Welch periodogram (Welch, 1967) with subwindows of 512 samples (5.12 s in length), a Hann window, and 50% overlap. The resulting PSDs were next integrated from 1 to 10 Hz, and the square roots of the results were taken, resulting in estimates every 5 min for the RMS pressure restricted to the 1–10 Hz frequency band.

The resulting time histories of the RMS pressures at each array are shown in Fig. 9. Plotted are the RMS pressure histories for the sensors that were functioning for enough of the 6 weeks to capture dynamics. The clear weather diurnal cycles are visible, for example, from March 13 through March 16. Under clear skies, turbulence in the atmospheric boundary layer is enhanced during the day, resulting from ground heating by the sun, and suppressed at night due to radiative cooling of the ground (Garratt, 1992; Stull, 2003). Periods of inclement weather are also visible, for example, from March 25 through March 29. During these periods, there is no clear diurnal cycle.

A statistical analysis of the RMS pressure time histories was performed. Probability density functions (PDFs) for the RMS pressures were estimated using the method of kernel

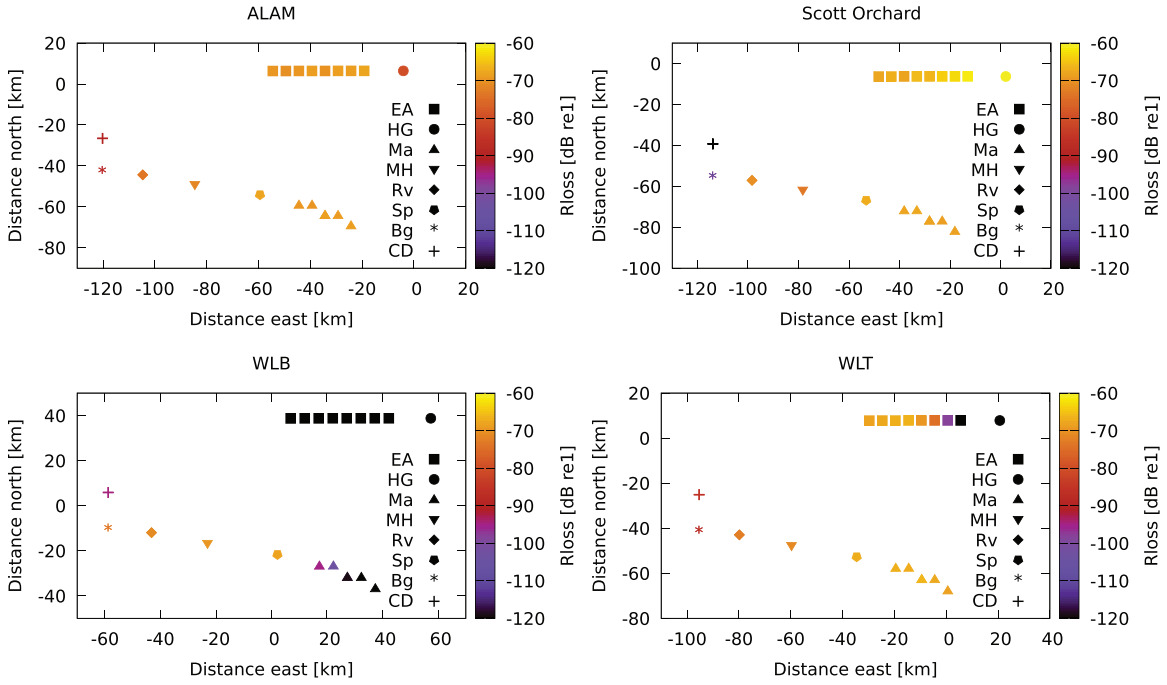

FIG. 8. Signal attenuation (reception loss) for ground-to-ground signal propagation at 4 Hz from each tornado track to each of the arrays.

density estimation (KDE; Parzen, 1962; Rosenblatt, 1956). For a given sensor, let p_j, where $j = 1, 2, 3, \ldots, N$, be the RMS pressures in dB, which are plotted in Fig. 9. The PDF, $P(p)$, for these RMS pressures is estimated by

$$P(p) \approx \frac{1}{Nh} \sum_{j=1}^{N} K\left(\frac{p - p_j}{h}\right),$$

where K is called the kernel function and is an approximate delta function in the sense that

$$\lim_{h \downarrow 0} \frac{1}{h} K\left(\frac{x}{h}\right) = \delta(x).$$

In this work, K is chosen to be the Epanechnikov kernel (Epanechnikov, 1969), which is given by $K(x) = \frac{3}{4}(1 - x^2)$ if $|x| \leq 1$, and $K(x) = 0$ if $|x| > 1$. h is called the width and taken here to be 2.5. The resulting PDFs, averaged over the active sensors in each array, are shown in the left panel of Fig. 10. In the right panel of Fig. 10, the cumulative distribution functions (CDFs) are displayed. These are defined as

$$C(p) = \int_{-\infty}^{p} P(p')\ dp'$$

and represent the fraction of the RMS pressures that were p or less.

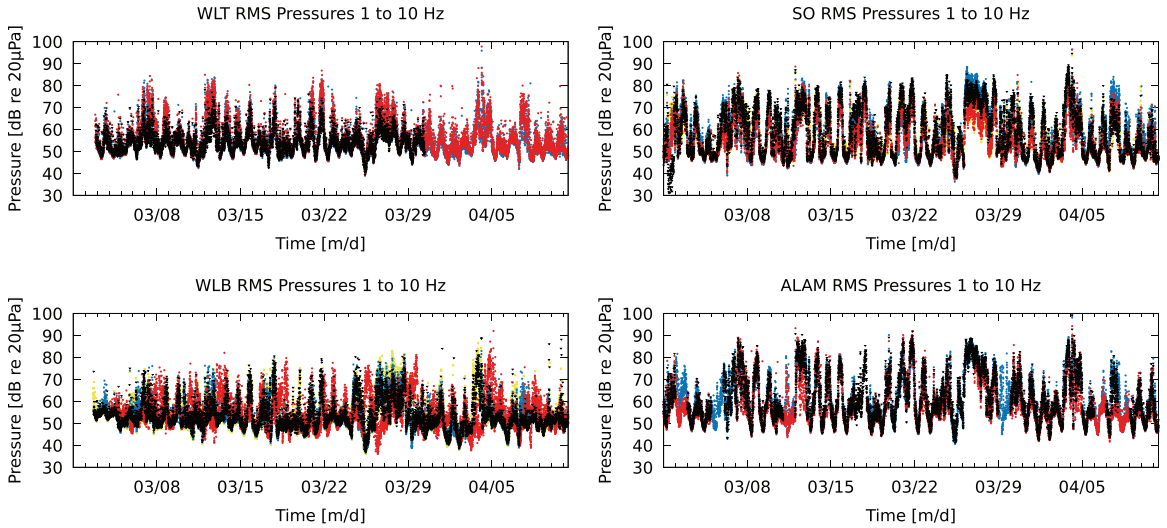

FIG. 9. RMS pressure in the 1–10 Hz frequency band at each of the arrays from March 1 through April 11, 2018. The results from all the sensors at each array that were functioning for most of the time period are plotted. The RMS pressures were computed in 5 min intervals.

https://doi.org/10.1121/10.0028815

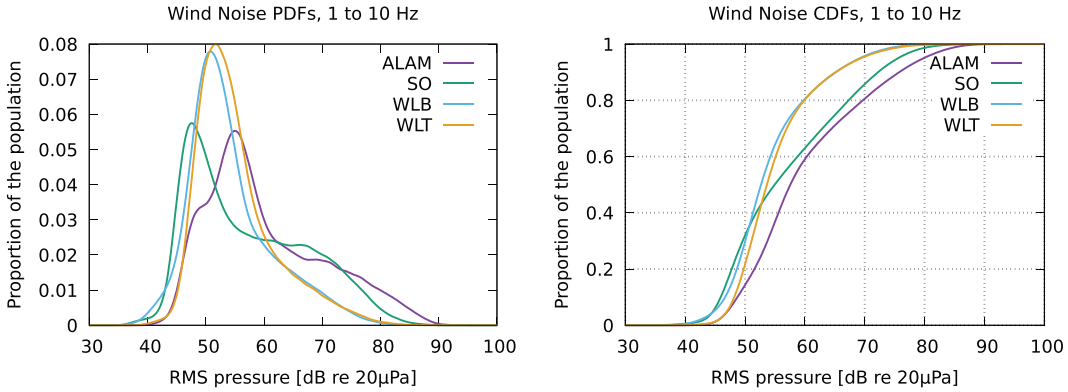

FIG. 10. Comparisons of the estimated PDFs and CDFs of the RMS pressures from Fig. 9 in the 1–10 Hz frequency band at each of the arrays.

The large peaks in the 40–60 dB range, observed in the PDF estimates for all four arrays, reflect the quieter nighttime periods. At ALAM and SO, there is a greater frequency of higher noise levels than is observed at WLB and WLT, implying that ALAM and SO were noisier arrays in the 1–10 Hz band than WLB and WLT. This is seen more clearly in the CDF plots, which show that at WLT and WLB, the noise levels were less than 70 dB about 95% of the time as compared to about 84% at SO and 80% at ALAM. The noise levels were less than 60 dB about 80% of the time at WLB and WLT but only about 60% of the time at SO and ALAM.

V. OBSERVATIONS AND DETECTIONS DURING THE TORNADO SWARM OF THE EVENING OF 19 MARCH 2018

A. General discussion

In this section, the data recorded at the arrays on the evening of March 19, 2018 are presented and discussed. In Fig. 11, the pressure fluctuation data collected at each of the four active arrays in the region are provided. A single sensor element from each array has been selected, and the data from that element is displayed. The data are arranged from bottom up in order of array passage time for the storm, and the passings are clearly visible in the large pressure fluctuations that accompany the storm. Most of these pressure fluctuations do not correspond to acoustic signals but rather are primarily turbulent pressure fluctuations, wind noise, associated with the passage of the storm. Any acoustic signals are buried in the wind noise. Array signal processing tools, to be discussed later, must be used to separate the acoustic signals from the turbulent noise and extract information about the signals.

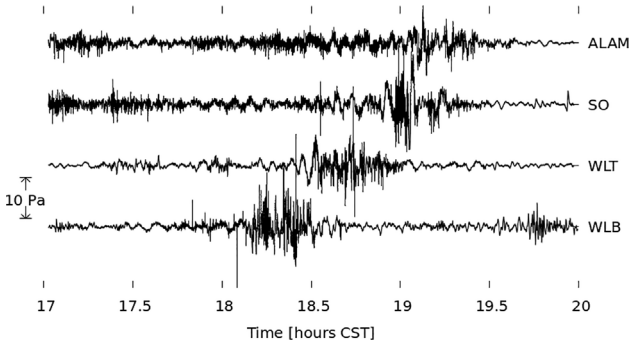

FIG. 11. Pressure fluctuation time series from a representative sensor element at each of the active arrays showing the passage of the March 19, 2018 storm.

In Fig. 12, the spectrograms corresponding to the time series depicted in Fig. 11 are displayed. The dramatic increase in broadband noise as the storm passes is observed. Examination of the spectrograms shows the broadband noise characteristic of high levels of atmospheric turbulence. Visible in the time series are occasional sharp impulsive signals that are also visible in the spectrograms. We hypothesize that these might be thunder. After the storm passed, a series of spectral lines are noticed undergoing Doppler shift, presumably from a helicopter. These are particularly prominent at the WLT array but are also visible at the SO and ALAM arrays. A persistent, faint spectral line is visible at the WLT array at about 21 Hz. This corresponds to some static source, perhaps from a nearby factory or machinery.

B. Detections

There are well-established methods for detecting an acoustic signal propagating across an array. Reviews can be found in Evers (2008), Jensen *et al.* (2000), and Marcillo *et al.* (2019). In addition to detections, most of these methods also provide estimates of the apparent bearing, also called back-azimuth, from the array toward the signal source as well as the trace velocities of the signal. For this application, potentially tracking multiple tornadoes, possibly in the presence of multiple anthropomorphic sources, a method that is robust to the presence of multiple continuous sources in a given frequency band is employed. There are several such methods (Cadzow, 1990; den Ouden *et al.*, 2020; Schmidt, 1986).

We use a recently developed extension of the multiple signal classification (MUSIC) method, which will be referred to as extended multiple signal classification (EMUSIC; Esfandiari *et al.*, 2019; Frazier *et al.*, 2019). The EMUSIC algorithm is a frequency domain algorithm similar in spirit to the more well-known MUSIC algorithm

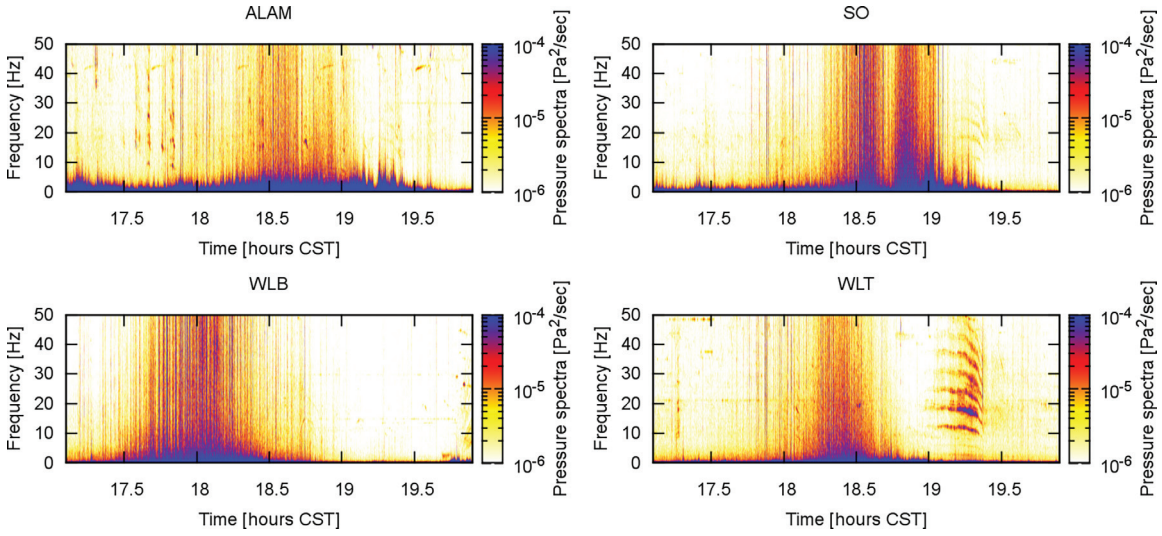

FIG. 12. Spectrograms corresponding to the time series presented in Fig. 11.

(Schmidt, 1986). Like MUSIC, EMUSIC is a subspace method (Cadzow, 1990) in that the vector space of array element responses is separated into two orthogonal subspaces, one of which is spanned by vectors that correspond to acoustic signals traversing the array while the other is spanned by vectors that correspond to noise. The dimension of the signal subspace is equal to the number of detectable signals incident on the array.

In traditional MUSIC, the separation into signal and noise subspaces is based on eigenvector decomposition of the array element cross spectral density matrix (XSDM; Bendat and Piersol, 1986) obtained by studying the eigendecomposition of the full XSDM. In EMUSIC, the eigendecomposition of a submatrix is studied explicitly, the submatrix containing only the off diagonal elements of the XSDM, $\mathrm{XSDM}_{\mathrm{off}}$. The advantages of analyzing the off diagonal submatrix are twofold. First, the noise levels are contained in the diagonal part of the XSDM such that with the EMUSIC algorithm noise levels are allowed to vary from sensor to sensor. Second, perhaps more importantly, it is shown in Esfandiari *et al.* (2019) that the decomposition into mutually orthogonal signal and noise subspaces is still respected by $\mathrm{XSDM}_{\mathrm{off}}$, and the eigenvalues of $\mathrm{XSDM}_{\mathrm{off}}$ corresponding to the noise subspace are all negative, all cluster together, and are widely separated from the eigenvalues corresponding to the signal subspace. Thus, EMUSIC provides a more robust estimate for the number of signals incident on an array. Further, estimates for the bearings toward and trace velocities of each signal can be obtained as can estimates for total signal power and total noise power. An exposition of the method can be found in Esfandiari *et al.* (2019), where it is also shown that the bearing estimates are more accurate than those obtained by traditional MUSIC.

Array coherence analysis was used to determine the frequency bands of greatest coherence. These were found to be 3–4.5 Hz for WLB and 4.5–6 Hz for WLT. For ALAM and SO, the coherence was generally poor; however, some coherence was observed in the 3–4.5 Hz band. It is not surprising that the frequencies of greatest coherence are not the same for all of the arrays even though the signals being tracked are presumably the same. The coherence is determined not only by the signals but also by array geometry, which is constrained by local topography and land availability, and noise levels at the arrays, which depends again on local topography as well as other factors known and unknown. Note that the aperture of the WLT array was smaller than that of the other arrays; see Fig. 2. In performing the data analysis, the bands of greatest coherence were taken as guides, augmented by trial and error.

The EMUSIC algorithm has been applied to the collected array data. Estimates for cross spectral density matrices are obtained by applying the Welch periodogram method (Welch, 1967) to user-specified time segments of the measured time series data. The time segments were 30 s in duration, and each sub-window was approximately 1.5 s duration. In each time segment, signals found by the EMUSIC algorithm are saved when the total SNR times the array gain (the square root of the number of sensors in the array) is greater than one. The resulting bearing (back-azimuth) and trace velocity estimates from the arrays to the sources are provided in Figs. 13 and 14, respectively. Estimates of the expected bearings corresponding to the tornado touchdown tracks published by the NWS are included in Fig. 13 for reference. Recall that the tornado designations and paths, per the NWS, are found in Table I and Fig. 1, respectively. The estimates of the total signal and noise power densities are displayed in Fig. 15.

Detections at ALAM and SO were sparse with scattered bearings and trace velocities. After the storm passed, noise levels dropped significantly and detections at SO revealed what appear to be stationary sources to the southwest with trace velocities clustering at about 350 m/s. Referring to Fig. 8, one sees that ALAM was well placed to detect signals emitted from all of the reported tornadoes. Similarly, SO is predicted to have been ensonified by all of the

https://doi.org/10.1121/10.0028815

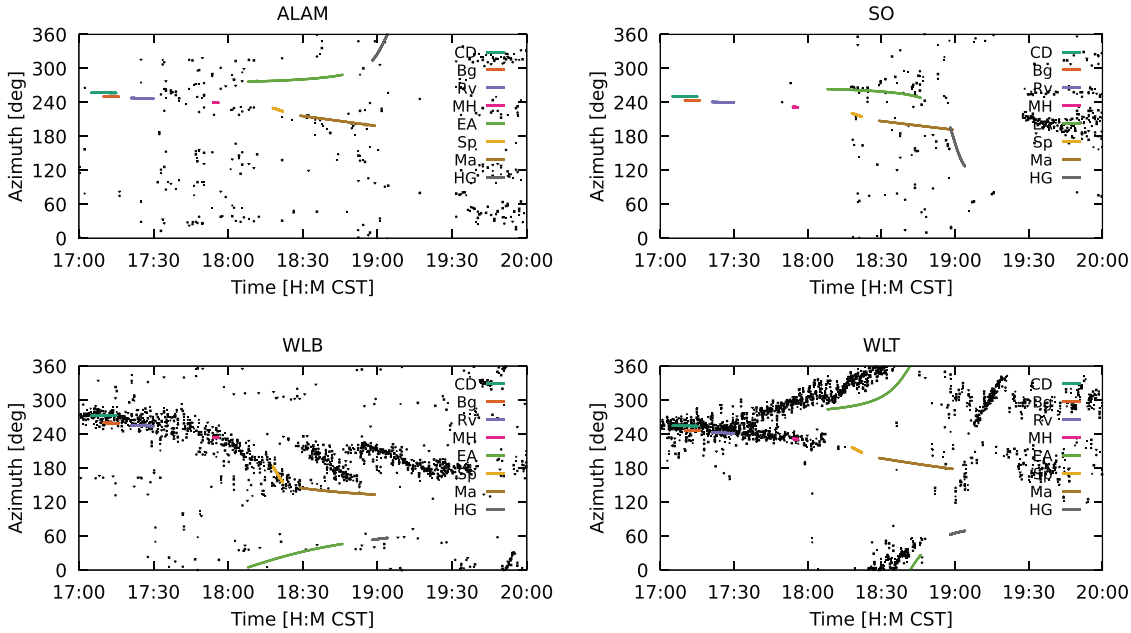

FIG. 13. Bearings to the observed tornadoes determined by infrasound array processing (March 19, 2018). The expected bearing estimates obtained from the NWS published touchdown tracks are also provided.

tornadoes except CD and Bg. As observed in Fig. 10, ALAM and SO were plagued with high wind noise levels. This likely explains the sparsity of the detections.

Figure 8 shows that WLB is predicted to have been ensonified by signals from Bg, Rv, and Sp. CD and Ma, on the beginning of the track, are predicted to have been in the ensonified/shadow zone transition and, thus, were borderline. WLB is predicted to have been in shadow zones for Ma after the first 5–10 km of its track, and for EA and HG, along the entirety of their tracks. WLT is predicted to have been ensonified by signals from all of the tornadoes except for EA at the end of its track and HG. The detections at WLB and WLT produced well-defined tracks of bearings consistent with the bearings for the tornadoes that are predicted to have ensonified those arrays. The trace velocities corresponding to these tracks were consistent with them being acoustic arrivals. At WLB, the trace velocities start at about 350 m/s and then increase as the tornadoes pass the array to the south. At WLT, however, the estimated trace velocities at WLT appear to be biased upward, beginning at about 375 m/s and increasing slightly as the EA tornado passed the array to the north. The increase in the trace velocities at

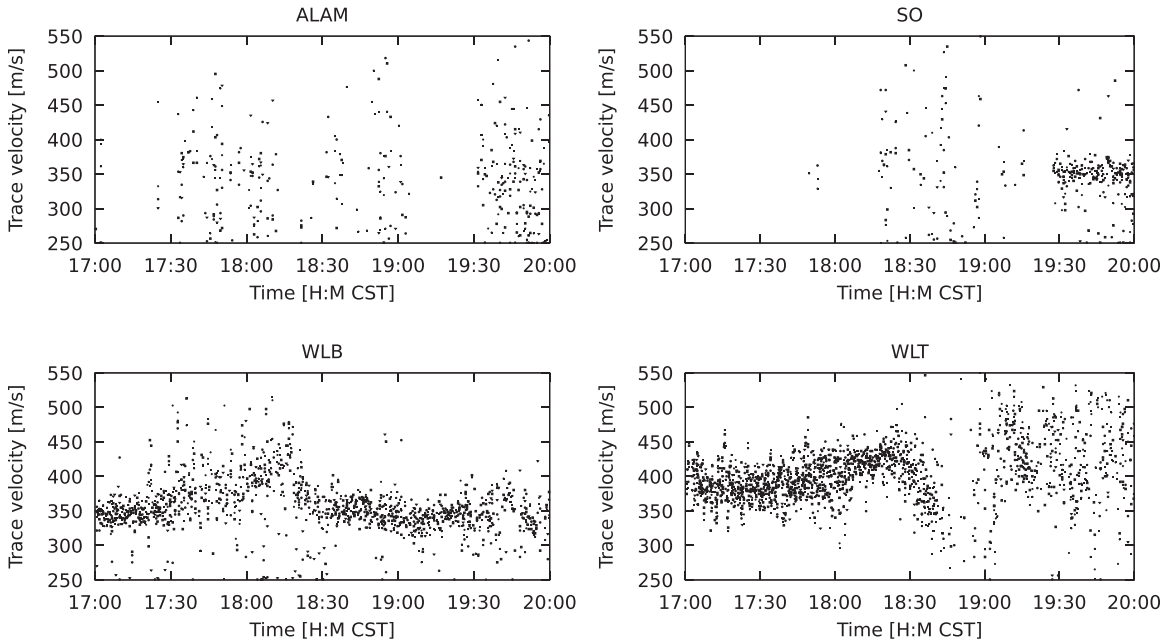

FIG. 14. Acoustic trace velocities corresponding to the bearings in Fig. 13.

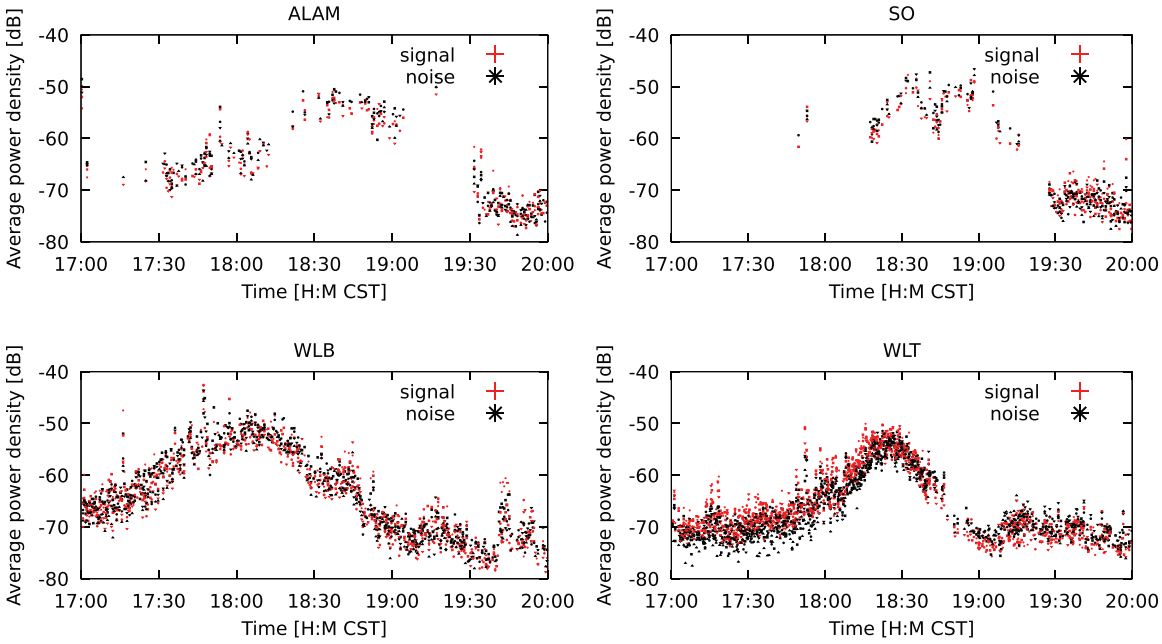

FIG. 15. Signal power versus noise power estimates at the arrays (March 19, 2018).

WLB suggest an elevated source; however, the string of tornadoes was 20 km or more from WLB, making it unlikely that this increase was the result of an elevated source in the tornado itself. We think it more likely that as the storm passed by, the trace velocity estimates became corrupted by nearby elevated sources such as thunder. A similar statement applies to the trace velocity estimations at WLT. This warrants further investigation as does the upward bias in the trace velocity estimations at WLT.

There is a long southward curving track observed in the WLB and WLT analyses from 17:00 CST to about 18:30 for WLB and about 18:00 for WLT. For WLB, it appears to comprise CD, Bg, Rv, MH, SP, and the very beginning of the Ma track, which is consistent with the propagation model predictions. For WLT, it appears to comprise CD, Bg, Rv, and MH, also consistent with the propagation model predictions. The WLT data analysis shows another bearing track emerging at about 17:30 from a source to the north of WLT and ending at about 18:45. The WLB data show two additional tracks bearing from the south-southwest to directly south, one from about 18:30 until 19:00 and the other from about 18:45 until 19:45. These might have been from storm cells passing by further to the south that are visible in the radar images (Fig. 4). These signals were not detected at WLT even though propagation modeling would suggest that WLT would have been ensonified. Consulting Fig. 15, one sees that these signal levels at WLB were not very strong and, hence, could have been obscured by noise at WLT. After the storm passed WLT, a track was detected at WLT from what appears to be a rapidly moving object from about 19:10 through 19:20. These could be the bearings to the source of the helicopter-like signal observed in the spectrogram shown in Fig. 12. From about 19:20 on, some scattered bearings to what could be two stationary sources are seen at WLT, the more southerly pointing of which is consistent with the similar bearing tracks noticed at SO from 19:30 on and would be consistent with a stationary source located between the cities of Madison and Huntsville.

There are several differences between the acoustic bearing tracks and the bearings to the NWS published tracks. One difference is that the bearings to CD and Bg were about 10° from WLB and WLT, which is too small to have been resolved with these array geometries and data processing method. As a consequence, the bearings to CD and Bg merged into a single track.

Less straightforward to explain is the acoustic bearings' bridging of the NWS reported tornado touchdowns. A single track connects CD, Bg, Rv, MH, and SP at WLB and CD, Bg, Rv, and MH at WLT. The reasons underlying this bridging warrant future investigation; at this point, one can only conjecture. It could be that CD, Bg, Rv, MH, and SP were, in fact, a single tornado that lifted off the ground several times or only produced limited ground damage that prevented the NWS investigators from discerning the entire track (Goudeau, 2018). Another possibility is that there was a supercell that radiated an infrasonic signal and spawned several tornadoes as it passed.

Finally, there are discrepancies between the bearing track from WLT to the EA tornado. For one thing, the acoustic track begins over a half hour before the NWS published touchdown. For another thing, when they do coincide spatially, the acoustic track lags behind NWS track by 10–15 min. It is possible that the discrepancy lies in the NWS published touchdown times, which are rapidly estimated from cells of high vorticity in the radar images. In fact, a more careful study of the radar images (Iowa State University Department of Agronomy, 2024) suggest that the

https://doi.org/10.1121/10.0028815

acoustic tracks, in this case, might be more accurate. This conjecture is consistent with the propagation transmission and reception loss estimates shown in Figs. 7 and 8. These are based on the tornado track obtained from the NWS published touchdown times and locations. In contrast to the acoustic track, the propagation models depict that by 18:35, the WLT array was passing into the acoustic shadow zone relative to the EA tornado locations. By 18:40, EA should not have been detectable at all. In contrast, the data processing shows a clear bearing track from WLT to EA through to the end of its path at about 18:45.

VI. NON-TORNADIC STORM CELLS

On the afternoon of March 19, 2018, prior to the passage of the storm front that produced the swarm of tornadoes whose infrasonic signals we have been studying, several storm cells of high vorticity passed across northern Alabama. Radar images from 1330, 1430, 1530, and 1630 CST are shown in Fig. 3. In the last image, the squall line that spawned the swarm of tornadoes is visible as it crosses northeastern Mississippi and begins to enter Alabama.

Severe thunder storm warnings were issued across the region, and at 13:40 CST, based on radar observations, a tornado warning was issued for Colbert County, Alabama in the northwest corner of the state (Iowa State University Department of Agronomy, 2024; U.S. Weather Services, 2018). The high vorticity storm cell that spawned the warning is visible in the radar images in Fig. 3 traveling east just south of Florence, Alabama near the Alabama/Tennessee state line. It begins as the westernmost of a string of high vorticity cells and intensifies as the other cells diminish in strength. It finally passes out of Alabama over the point where Alabama, Georgia, and Tennessee meet. Despite the warning, no confirmed tornado touchdowns were reported during the passage of this front.

In Fig. 16, the paths of the storm cells with base Doppler radar reflectivity of about 50 dB or higher are shown relative to the placements of the infrasound sensor arrays. The approximate path of the high vorticity cell that spawned the tornado warning is displayed in red. The paths of the other cells are shown in gray. The points along the paths are locations of cells every 10 min and the times, in CST, are indicated on the hours and half hours. Note that the points for each cell have a unique shape: red circle, gray box, triangle, and inverted triangle. Figure 17 shows the results of the analyses of the data for the WLB and WLT arrays, and Fig. 18 shows bearings and ranges to the various storm cells.

A clear and tight bearing track was observed at WLB. It begins at about 13:00 and continues for an hour until about 14:00. It shows a source beginning directly to the west of WLB and then traversing past the array to the north. The signal power density starts out quite low but then increases to a maximum sometime between 13:50 and 14:00. After 14:00, the detections become scattered and less distinct. Consideration of Figs. 16 and 18 strongly suggests that the source of the signals producing this tight bearing track was the cell that produced the tornado warning, marked in red in Figs. 16 and 18. It passed by WLB to the north at about 14:10 at a distance of about 20 km. It then passed to the east into acoustic shadow zone of WLB. A less distinct track can be observed between 12:00 and 12:45, which has bearings consistent with those for the portions of the tracks of the other three high vorticity cells from which one might expect signals to propagate to WLB.

The results of the WLT data analysis are less clear-cut. Between 12:00 and about 12:30, two bearing tracks are noticed. One, the more well defined of the two, tracks bearings to the west with a slight upturn, which is consistent with the bearings to the storm cell that traversed the northwest corner of Alabama, marked in the plots with the gray

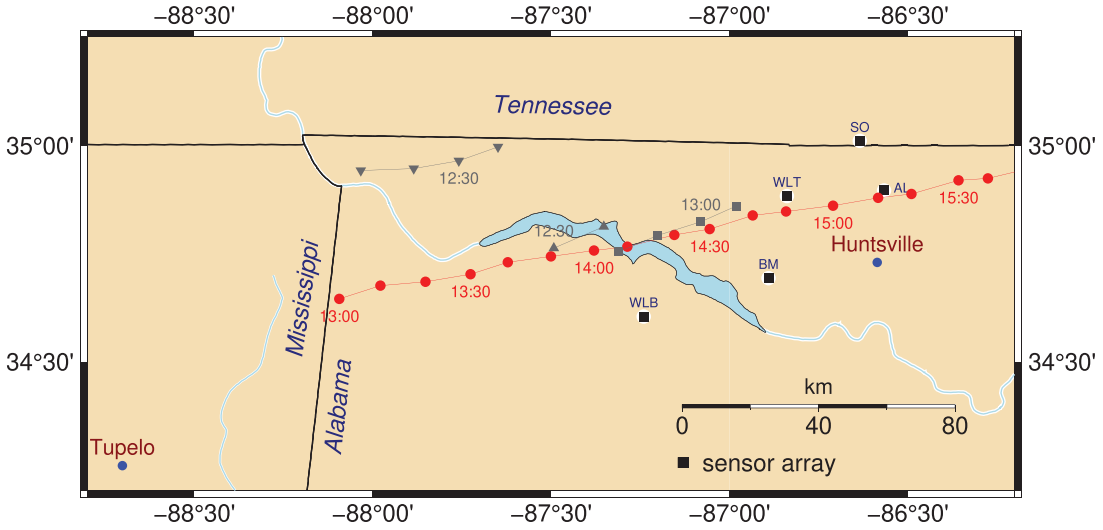

FIG. 16. Tracks of storm cells of high vorticity (50 dB or greater Doppler radar reflectivity) crossing northern Alabama on the afternoon of March 19, 2018. The positions of the deployed infrasound sensor arrays are indicated as well. One of the cells produced a tornado warning. Its path is in red. The paths of the others are in gray. The points along the paths are at 10 min intervals and the times are in CST.

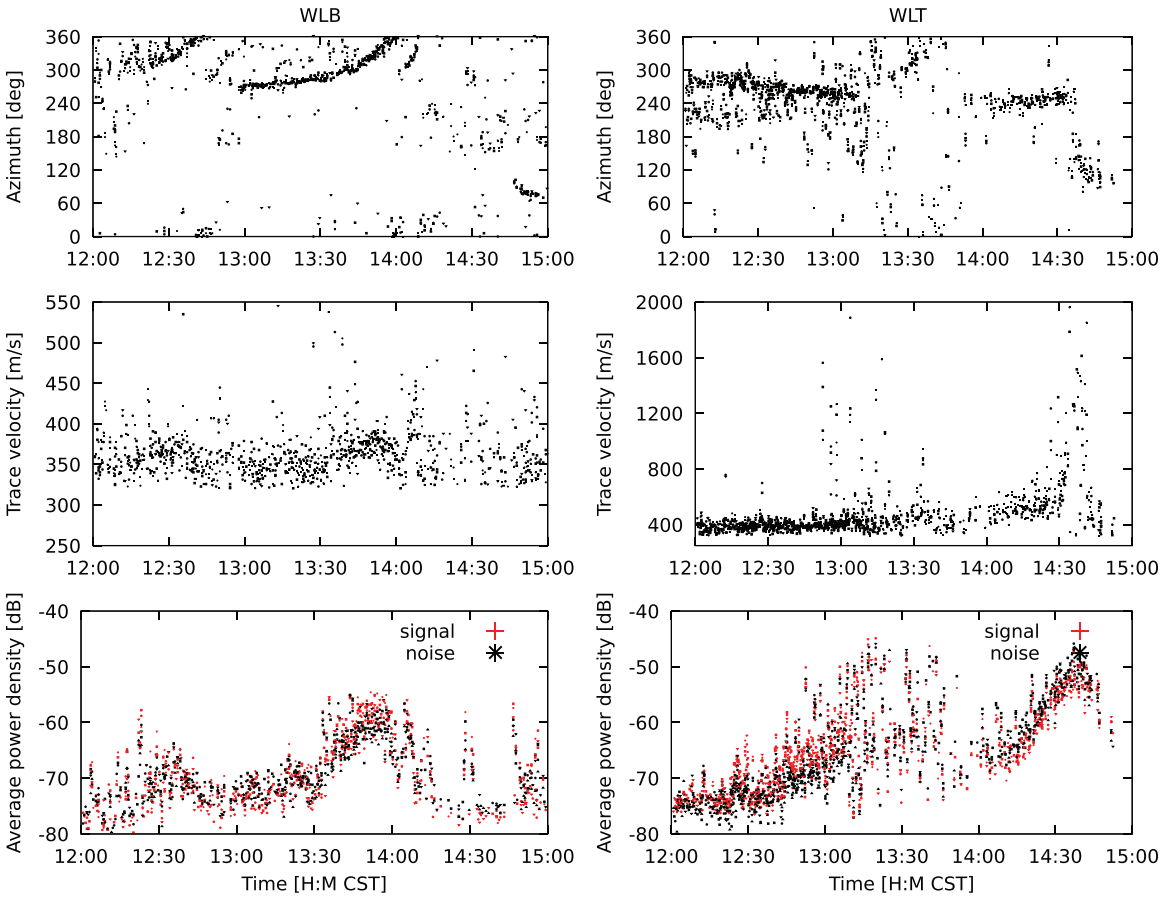

FIG. 17. Results of array processing for data collected at WLB and WLT on the afternoon of March 19, 2018. The three rows, from top to bottom, contain the bearing estimates, trace velocities, and signal and noise power densities, respectively.

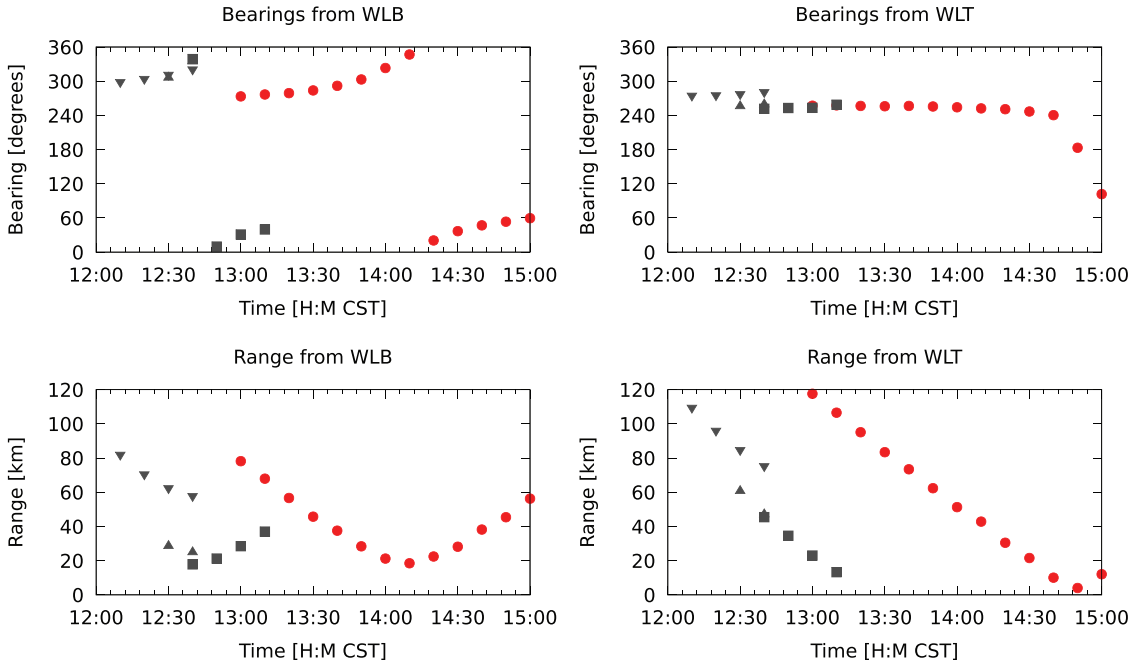

FIG. 18. Bearings to (upper row) and distance from (lower row) the centers of the high vorticity storm cells that traversed northern Alabama during the afternoon of March 19, 2018. The red dots indicate the cell that produced the tornado warning. The gray symbols are the other cells. The shapes of the symbols correspond to those in Fig. 16.

https://doi.org/10.1121/10.0028815

inverted triangle. The other, more scattered path, tracks a stationary bearing to the southwest, which is consistent with the stationary bearings observed in the data after the storm passed and discussed in Sec. V. Again, we hypothesize that these are anthropomorphic in origin. By 12:45 and continuing until about 13:45, a single well-formed dominant track emerged, surrounded by detections with more scattered bearings. The well-formed track followed bearings to the west-southwest, which is consistent with bearings to all three more southern storm cells: those indicated by the red circles, gray boxes, and gray triangles in the plots. The power densities at WLT began increasing at about 12:30 and became quite large between 13:15 and 13:45, during which time storm cells passed directly over the array, and detections became quite scattered. At 14:00, a clear bearing track is seen to be consistent with signals from the high vorticity cell, indicated by the red circles. This cell appears to have passed over WLT between 14:40 and 14:45, resulting in high noise levels and scattered detections. A short track of bearings to the east-southeast emerged during this period and are consistent with bearings to the high vorticity cell once it passed WLT, after which it presumably entered the WLT acoustic shadow zone. The estimated trace velocities increase steeply during this period, which is consistent with a storm passing overhead; however, the caveats discussed in Sec. V still apply.

These results bring into question the uniqueness of infrasonic signals from tornadoes because signals were received from high vorticity cells that, presumably, did not spawn tornadoes. One distinction is the source strength. Consider the power densities at WLB. Unlike WLT, these were not complicated by the passage overhead of storm cells. Comparing power densities to those observed from the verified tornadoes (see Fig. 15), the signal from the cell that spawned the tornado warning was between 5 and 10 dB quieter than those from the verified tornadoes at comparable distances. The differences in levels depend on which part of the track one is considering, where the smaller differences are at the closest point of approach. This needs to be verified by much more data collection and analysis; however, it does suggest that vorticity plays a significant role in infrasound radiation as the clearest signal received during the afternoon was from the highest vorticity cell, which, in turn, was weaker than the signals received from the verified tornadoes later that evening.

VII. CONCLUSIONS AND DISCUSSION

We have presented results of extensive analysis of infrasound data collected on four sensor arrays that were active in Central Alabama on March 19, 2018 during the passage of two quasi-linear convective systems of storm cells (more colloquially referred to as squall lines). This particular storm was singled out for analysis because on the evening of March 19, several of the storm cells produced tornadoes, eight of which were confirmed by the NWS. During the afternoon, one of the cells was observed to have sufficient vorticity to warrant the issuing of a tornado warning, but there was no verified tornado touchdown. Similar analyses have been performed on other tornado producing storms with similar results (Frazier *et al.*, 2017; Goudeau, 2018; Goudeau *et al.*, 2018); however, much more effort went into the data analysis presented here, and the analyses performed were more complete. The March 19, 2018 storm was focused on because of the extreme tornadic activity.

The analysis included bearing of arrival and average power density estimation using techniques specifically designed to handle multiple, simultaneous infrasound sources. Because there are so many potential sources of infrasound in storms, rather than the usual focus on signal detection, the focus here is on well-formed tracks of bearing estimates as would be expected from infrasound radiated continuously by moving tornadoes. The best results were obtained in the frequency range between 1 and 6 Hz. The upper frequency might have been limited by the geometry of the sensor arrays; the inter-sensor spacing was too large with aperture of 100 m for the analysis of frequencies higher than 6 Hz. The lower frequency might have been limited by the size of the wind screens; these type of wind screens become effective at 2 Hz and above.

The vertical atmospheric profiles of wind and temperature in the geographic area have a dramatic influence on the ability to detect distant sound sources. Using time varying and range dependent atmospheric wind and temperature profiles, a detailed signal propagation analysis was undertaken for propagation from each tornado to each of the sensor arrays to determine which tornado signals should have been detected.

Examination of the local noise at each array was undertaken to complement the signal propagation analysis. A statistical method for evaluating the noise levels at a given site was developed and is based on using long term data collection to estimate the CDF for band limited noise generated RMS pressure. It was found that two of the arrays were considerably noisier than the other two, producing lower SNR at the noisier arrays. One of these arrays, SO, was deployed in a fruit orchard. We suspect that the widely spaced trees generate turbulence that raises the local noise levels.

At the quieter arrays, for the documented tornadoes, when SNR analysis suggested that bearing tracks from a tornado should have been detected, they were. Further, the estimated bearings to the tornadoes were shown to be consistent with the tracks published by the NWS with two significant differences. One difference is that in some cases, the bearings estimated from the infrasound signal analysis seem to extend the tracks determined by the NWS and even connect some of them into a single, longer track; see Fig. 13. The other difference is that in one case, the infrasound derived bearings indicated different touchdown times than those published by the NWS. This all bears further investigation.

In general, when noise levels were low, prior to and after the passage of the storm fronts, continuous and stationary signals were detected whose bearings pointed toward nearby cities. These signals are presumably from factories

or other such facilities but were easily identifiable and too low in signal level to interfere with the tornado signal detections. A signal from what we suspect was a helicopter was also detected in the evening after the storm had passed.

In the afternoon prior to the passage of the squall line that spawned the swarm of tornadoes on the evening of March 19, 2018, a line of high vorticity cells passed by. One of the cells had high enough vorticity for the NWS to issue a tornado warning, although no verified tornado touchdown was reported. Data collected during the passage of these cells were analyzed in the 1–6 Hz frequency band. The analysis results were consistent with an infrasonic signal similar to those observed from tornadoes having been radiated from the region near this high vorticity cell, albeit with lower intensity than that for the signals received from the verified tornadoes.

We also noted that nearby thunder often reduced the quality of the bearing tracks when distant tornadoes were on the ground; this motivates further investigation into techniques to better suppress the influence of undesirable acoustic transients. It should be noted that such contamination will only affect a single array in the deployed network.

These results have motivated several changes in our strategy for deployment of networks of infrasound sensing arrays for the purpose of tornado monitoring. Based on the signal propagation analysis, in subsequent deployments, the networks have been designed with arrays distributed more or less in a line to the northeast of the region being monitored rather than in a cluster about a given region. Sensor element spacings have been reduced by half (from 100 m aperture down to 50 m aperture) to enable better analysis results at higher frequencies (and correspondingly smaller acoustic wavelengths). Finally, it is clear that a critical element in future deployments must be the location of sites with low intrinsic wind noise levels.

ACKNOWLEDGMENTS

First, we would like to thank the landowners who allowed us to deploy arrays on their properties. We gratefully acknowledge enlightening discussions with Kevin Knupp at the University of Alabama and thank Ernst Cebert at Alabama A&M for assistance in monitoring the health of our array. This work was supported in part by funding from NOAA Grant Nos. NA17OAR4590168, NA18OAR4590305, and NA19OAR4590339.

AUTHOR DECLARATIONS

Conflict of Interest

The authors have no conflicts to disclose.

DATA AVAILABILITY

The data that support the findings of this study are available from the corresponding author upon reasonable request.

Akhalkatsi, M., and Gogoberidze, G. (**2009**). "Infrasound generation by tornadic supercell storms," Q. J. R. Meteorol. Soc. **135**(641), 935–940.
Akhalkatsi, M., and Gogoberidze, G. (**2011**). "Spectrum of infrasound radiation from supercell storms," Q. J. R. Meteorol. Soc. **137**(654), 229–235.
Arnold, R. T., Bass, H. E., and Bolen, L. N. (**1976**). "Acoustic spectral analysis of three tornadoes," J. Acoust. Soc. Am. **60**(3), 584–593.
Bedard, A. (**2005**). "Low-frequency atmospheric acoustic energy associated with vortices produced by thunderstorms," Mon. Weather Rev. **133**(1), 241–263.
Bendat, J., and Piersol, A. G. (**1986**). *Random Data: Measurement and Analysis Procedures* (Wiley, New York).
Bowman, J. R., Baker, G. E., and Bahavar, M. (**2005**). "Ambient infrasound noise," Geophys. Res. Lett. **32**(9), L09803, https://doi.org.//10.1029/2005GL022486.
Cadzow, J. A. (**1990**). "Multiple source location-the signal subspace approach," IEEE Trans. Acoust, Speech, Signal Process. **38**(7), 1110–1125.
Collins, M. D., and Siegmann, W. L. (**2019**). *Parabolic Wave Equations with Applications* (Springer, New York).
den Ouden, O. F., Assink, J. D., Smets, P. S., Shani-Kadmiel, S., Averbuch, G., and Evers, L. G. (**2020**). "Clean beamforming for the enhanced detection of multiple infrasonic sources," Geophys. J. Int. **221**(1), 305–317.
Elbing, B. R., Petrin, C., and Van Den Broeke, M. S. (**2018**). "Monitoring infrasound from a tornado in Oklahoma," J. Acoust. Soc. Am.**143**(3), 1808.
Epanechnikov, V. A. (**1969**). "Non-parametric estimation of a multivariate probability density," Theory Probab. Appl. **14**(1), 153–158.
Esfandiari, M., Vorobyov, S. A., Alibani, S., and Karimi, M. (**2019**). "Non-iterative subspace-based DOA estimation in the presence of nonuniform noise," IEEE Signal Process. Lett. **26**(6), 848–852.
Evers, L. G. (**2008**). "The inaudible symphony: On the detection and source identification of atmospheric infrasound," Ph.D. thesis, TU Delft, Delft, Netherlands.
Frazier, G., Waxler, R. M., and Hetzer, C. (**2024**). "Predicting infrasonic wind noise levels using local topographic features," J. Acoust. Soc. Am. **155**(3_Supplement), A116.
Frazier, W. G., Talmadge, C. L., Hetzer, C., and Waxler, R. M. (**2019**). "Estimating multiple bearings-of-arrival from tornadic storms using the complex Wishart distribution," J. Acoust. Soc. Am. **145**(3), 1867.
Frazier, W. G., Talmadge, C., Park, J., Waxler, R., and Assink, J. (**2014**). "Acoustic detection, tracking, and characterization of three tornadoes," J. Acoust. Soc. Am. **135**(4), 1742–1751.
Frazier, W. G., Talmadge, C. L., Waxler, R., Knupp, K. R., Goudeau, B., and Hetzer, C. H. (**2017**). "Investigation and characterization of acoustic emissions of tornadoes using arrays of infrasound sensors," in *AGU Fall Meeting Abstracts*, Vol. 2017, pp. NH51B–0130.
Garratt, J. (**1992**). *The Atmospheric Boundary Layer* (Cambridge University Press, New York).
Georges, T., and Greene, G. E. (**1975**). "Infrasound from convective storms. Part IV. Is it useful for storm warning?," J. Appl. Meteor. **14**(7), 1303–1316.
Georges, T. M. (**1973**). "Infrasound from convective storms: Examining the evidence," Rev. Geophys. **11**(3), 571–594, https://doi.org.//10.1029/RG011i003p00571.
Godin, O. A. (**1997**). "Reciprocity and energy theorems for waves in a compressible inhomogeneous moving fluid," Wave Motion **25**(2), 143–167.
Goudeau, B. (**2018**). "A case study on the usage and efficacy of infrasound monitoring arrays as a means of tornado detection," Master's thesis, The University of Alabama, Huntsville, AL.
Goudeau, B., Knupp, K. R., Frazier, W. G., Waxler, R., Talmadge, C., and Hetzer, C. (**2018**). "An analysis of tornado-emitted infrasound during the vortex-se field campaign," in *98th American Meteorological Society Annual Meeting*, January 6–11, 2018, Austin, TX.
Iowa State University Department of Agronomy (**2024**). "Iowa environmental mesonet," available at https://mesonet.agron.iastate.edu/GIS/apps/rview/warnings.phtml (Last viewed July 29, 2024).
Jensen, F. B., Kuperman, W. A., Porter, M. B., and Schmidt, H. (**2000**). *Computational Ocean Acoustics* (Springer, New York), Chap. 10.
Mapbox (**2024**). "Mapping and moving the world with intelligent location," available at https://www.mapbox.com/about/maps/ (Last viewed September 12, 2024).

Marcillo, O., Arrowsmith, S., Charbit, M., and Carmichael, J. (**2019**). "Infrasound signal detection: Re-examining the component parts that makeup detection algorithms," in *Infrasound Monitoring for Atmospheric Studies*, edited by A. Le Pichon, E. Blanc, and A. Hauchecorne (Springer, Cham, Switzerland), pp. 249–271.

Markowski, P., and Richardson, Y. (**2011**). *Mesoscale Meteorology in Midlatitudes* (Wiley, West Sussex, UK).

Marty, J. (**2019**). *The IMS Infrasound Network: Current Status and Technological Developments* (Springer, Cham, Switzerland), pp. 3–62.

NCEP/NWS/NOAA (**2015**). "NCEP GDAS/FNL 0.25 degree global tropospheric analyses and forecast grids," available at https://doi.org/10.5065/D65Q4T4Z, updated daily (Last viewed July 29, 2024).

OpenStreetMap (**2024**). "OpenStreetMap," available at https://www.openstreetmap.org/copyright/ (Last viewed September 12, 2024).

Parzen, E. (**1962**). "On estimation of a probability density function and mode," Ann. Math. Statist. **33**(3), 1065–1076.

Raspet, R., Abbott, J.-P., Webster, J., Yu, J., Talmadge, C., Alberts, K., Collier, S., and Noble, J. (**2019**). "New systems for wind noise reduction for infrasonic measurements," in *Infrasound Monitoring for Atmospheric Studies*, edited by A. Le Pichon, E. Blanc, and A. Hauchecorne (Springer, Cham, Switzerland), pp. 91–124.

Rinehart, H. S., Clark, C., Gray, M., and Dillion, K. (**2012**). "Application of a blind source separation algorithm for the detection and tracking of tornado-generated infrasound emissions during the severe weather outbreak of 27 April 2011," J. Acoust. Soc. Am. **132**(3), 2074.

Rosenblatt, M. (**1956**). "Remarks on some nonparametric estimates of a density function," Ann. Math. Statist. **27**(3), 832–837.

Scamfer, L. T., and Anderson, J. F. (**2023**). "Exploring background noise with a large-N infrasound array: Waterfalls, thunderstorms, and earthquakes," Geophys. Res. Lett. **50**(24), e2023GL104635, https://doi.org.//10.1029/2023GL104635.

Schecter, D. A. (**2011**). "A method for diagnosing the sources of infrasound in convective storm simulations," J. Appl. Meteorol. Climatol. **50**(12), 2526–2542.

Schecter, D. A. (**2012**). "A brief critique of a theory used to interpret the infrasound of tornadic thunderstorms," Mon. Weather Rev. **140**(7), 2080–2089.

Schecter, D. A., and Nicholls, M. E. (**2010**). "Generation of infrasound by evaporating hydrometeors in a cloud model," J. Appl. Meteorol. Climatol. **49**(4), 664–675.

Schmidt, R. (**1986**). "Multiple emitter location and signal parameter estimation," IEEE Trans. Antennas Propagat. **34**(3), 276–280.

Schmitter, E. D. (**2010**). "Modeling tornado dynamics and the generation of infrasound, electric and magnetic fields," Nat. Hazards Earth Syst. Sci. **10**(2), 295–298.

Skamarock, W. C., Klemp, J. B., Gill, D. O., Barker, D. M., Duda, M. G., Huang, X., Wang, W., and Powers, J. G. (**2019**). "A description of the advanced research WRF model version 4," National Center for Atmospheric Research, Boulder, CO, 145 pp.

Stull, R. B. (**2003**). *An Introduction to Boundary Layer Meteorology* (Springer Science and Business Media, Kluwer, Dordrecht).

Talmadge, C., and Waxler, R. (**2016**). "Infrasound from tornados: Theory, measurement, and prospects for their use in early warning systems," Acoust. Today **12**(1), 43–51.

U.S. Weather Services (**2018**). "March 19, 2018 tornadoes and large hail," available at https://www.weather.gov/hun/ (Last viewed July 29, 2024).

Waxler, R., and Assink, J. (**2019**). "Propagation modeling through realistic atmosphere and benchmarking," in *Infrasound Monitoring for Atmospheric Studies*, edited by A. Le Pichon, E. Blanc, and A. Hauchecorne (Springer, Cham, Switzerland), pp. 509–549.

Waxler, R., Assink, J., and Velea, D. (**2017**). "Modal expansions for infrasound propagation and their implications for ground-to-ground propagation," J. Acoust. Soc. Am. **141**(2), 1290–1307.

Waxler, R., Hetzer, C., Assink, J., and Velea, D. (**2021**). "chetzer-ncpa/ncpaprop-release: Ncpaprop v2.1.0," available at https://github.com/chetzer-ncpa/ncpaprop-release (Last viewed September 12, 2024).

Welch, P. (**1967**). "The use of fast Fourier transform for the estimation of power spectra: A method based on time averaging over short, modified periodograms," IEEE Trans. Audio Electroacoust. **15**(2), 70–73.